International Journal of Heat and Fluid Flow 115 (2025) 109791

Contents lists available at ScienceDirect

International Journal of Heat and Fluid Flow

journal homepage: www.elsevier.com/locate/ijhff

Turbulent heat transfer and secondary flows in a non-uniformly heated pipe with temperature-dependent fluid properties

A. Antoranz [a,b], O. Flores [a], M. García-Villalba [c,*]

[a] Dpto. Ing. Aeroespacial, Universidad Carlos III de Madrid, 28911 Leganés, Spain
[b] ITP Aero, 28108 Alcobendas, Spain
[c] Institute of Fluid Mechanics and Heat Transfer, TU Wien, Vienna, Austria

ARTICLE INFO

Keywords:
Direct numerical simulation
Heat transfer
Pipe flow
Turbulence
Temperature-dependent fluid properties

ABSTRACT

The influence of temperature-dependent fluid properties in a turbulent pipe flow with sinusoidal heat flux boundary conditions is studied. Four cases with increasing sensitivity to temperature variations, representative of molten salts in solar heat receivers, are calculated by means of direct numerical simulation. The computations have been performed with a reference friction Reynolds number equal to 180 and a reference Prandtl number equal to 0.7. It is found that the fluid properties variations result in an enhancement (damping) of the flow and temperature fluctuations on the cold (hot) side of the pipe. Small secondary motions of Prandtl second kind are found to occur with a significant impact on the vertical heat flux, accounting for one third of the total heat flux in the most sensitive case. Finally, the effect of the variable fluid properties in integral quantities like friction coefficient and Nusselt number is quantified.

1. Introduction

Latest developments in the technology of Solar Thermal Collectors, improving efficiency and operational costs, has risen the interest on using renewable energy coming from the sun for industrial purposes. In particular, Solar Power Tower systems utilize sun-tracking mirrors, called heliostats, to reflect solar radiation onto a receiver and heat the working fluid, typically a molten salt. This heat is accumulated and used on demand to create steam to move a turbine producing electricity (Merchán et al., 2022).

For the application of a Central Solar Receiver using molten salts in pipes of typically 25 mm diameter, the working conditions are characterized by flow bulk velocities of about 1–3 m/s and bulk temperatures in the range of 500–750 K. At these conditions, and depending on the salt used (Solar Salt, Hitec or Hitec XL for example), the typical working range for the bulk Reynolds number is $Re_b = 2U_bR/\nu = 5 \cdot 10^3$–$5 \cdot 10^4$, where U_b is the bulk velocity, R is the pipe radius and ν is the kinematic viscosity. The tube face exposed to the solar radiation receives a heat flux of order $q''_w \sim 1$ MW/m^2, while the opposite face is almost adiabatic. This highly non-uniform heat flux distribution produces significant circumferential temperature variations on the pipe wall, ranging from $\Delta T = 50$–250 K along the pipe (Rodríguez-Sánchez et al., 2014). In terms of working fluid properties variation, this temperature difference produces changes in density, ρ, of about 5–10%, in specific heat coefficient, C_p, of about 2–5%, in thermal conductivity, k, of about 10–30% and in dynamic viscosity, μ of about 100–200% from the hot face to the cold face. It is however unclear what is the impact of these fluid property variations on the heat transfer performance of the system.

In spite of their practical relevance, to the best of our knowledge there are no studies in the literature of pipe flow with variable fluid properties and circumferentially varying heat flux boundary conditions. Numerical studies of heat transfer in a pipe with homogeneous heating can be found in Piller (2005) and Redjem-Saad et al. (2007), among others, while the experimental study of circumferentially-varying heat flux are reported e.g. in Black and Sparrow (1967) or Quarmby and Quirk (1972). In previous works (Antoranz et al., 2015, 2018), the present authors reported DNS of pipe flow with circumferentially-varying heat flux with constant fluid properties. More recently, Straub et al. (2019) have also investigated the effect of azimuthally inhomogeneous heat flux in a pipe using liquid metals as the working fluid. Also, the influence of a sinusoidally-varying, periodic, thermal boundary condition in circumferential direction of a vertical turbulent pipe flow driven by the pressure gradient and buoyancy forces was studied by Dachwitz et al. (2023).

Regarding the studies on temperature-dependent fluid properties, the works of Zonta et al. (2012) and Lee et al. (2013), despite not being done for a pipe flow, are of application for our current analysis. Zonta et al. (2012) carried out direct numerical simulation (DNS) of a forced

* Corresponding author.
E-mail addresses: antonio.antoranz@uc3m.es (A. Antoranz), manuel.garcia-villalba@tuwien.ac.at (M. García-Villalba).

https://doi.org/10.1016/j.ijheatfluidflow.2025.109791
Received 20 August 2024; Received in revised form 21 February 2025; Accepted 22 February 2025

convection turbulent flow in a channel with anisotropic temperature-dependent viscosity and different channel walls temperature. Lee et al. (2013) reported DNS of a turbulent boundary layer over heated walls to investigate the effect of viscosity stratification. Both found a reduction of turbulence near the heated wall, where viscosity was lower. For a pipe flow, Sufrà and Steiner (2022) studied the effect of temperature depending material properties on heat and momentum transfer. They applied a constant averaged wall heat flux and considered separately the cases of heated and cooled wall. They reported significantly damped/enhanced turbulent motion caused by the increase/decrease of the viscosity with distance to the heated/cooled wall. Finally, for a fluid with variable properties in a pipe, high Prandtl number flow has been studied by Irrenfried and Steiner (2024).

In this paper, we perform DNS of a pressure-driven fully developed turbulent flow in a pipe, with sinusoidal heat flux boundary conditions, and with temperature-dependent viscosity and thermal diffusivity, representative of the conditions in the tubes of heat receivers in Solar Power Tower plants. Note that we simplify the problem by neglecting variations in fluid density and C_p and having a null net heat flux to the pipe. The main objective of this study is to analyze the influence of variable fluid properties on mean values and turbulence statistics in the heat transfer fluid. To that end, four different conditions are considered: a case with constant fluid properties and three cases with temperature-dependent fluid properties. Preliminary results were reported in Antoranz et al. (2020).

The structure of the paper is as follows. First, the governing equations and the boundary conditions are presented, together with a brief description of the computational setup and the definition of the cases of study. The results are presented and discussed next. First, the circumferential distributions on the pipe wall are reported. After that, we analyze the influence of varying fluid properties on the velocity and temperature statistics. We then focus on the secondary flows created due to the non-isotropic fluid properties and their effect on the heat fluxes. Finally, the impacts on the overall flow performance are quantified.

2. Computational setup

The governing equations are the Navier–Stokes equations for an incompressible flow with a constant pressure gradient, $\partial p/\partial z$, in the direction of the pipe axis, z, together with an advection–diffusion equation for the temperature (neglecting viscous energy dissipation). Note that in this case, the energy and momentum equations are coupled by the variation of viscosity with temperature.

The resulting system of equations is

$$\frac{\partial u_i}{\partial x_i} = 0, \tag{1}$$

$$\frac{\partial u_i}{\partial t} + u_j \frac{\partial u_i}{\partial x_j} = -\frac{1}{\rho}\frac{\partial p}{\partial x_i} + \frac{\partial}{\partial x_j}\left(\nu(T)\frac{\partial u_i}{\partial x_j}\right), \tag{2}$$

$$\frac{\partial T}{\partial t} + u_i \frac{\partial T}{\partial x_i} = \frac{\partial}{\partial x_i}\left(\alpha(T)\frac{\partial T}{\partial x_i}\right), \tag{3}$$

where repeated sub-indices indicate Einstein summation convention, $(x_1, x_2, x_3) = (x, y, z)$ are the three Cartesian coordinates and $(u_1, u_2, u_3) = (u_x, u_y, u_z)$ their corresponding velocity components. Temperature is designated by T, p is the pressure, $\nu = \mu(T)/\rho$ is the kinematic viscosity and $\alpha = k(T)/\rho C_p$ is the thermal diffusivity.

The system of Eqs. (1)–(3) is completed with appropriate boundary conditions on the pipe surface: velocity is zero at the wall, and the wall-normal temperature gradient is given by an imposed sinusoidal heat flux distribution

$$q''_w(\theta) = \pi \overline{q}''_w \sin\theta = -\rho C_p \alpha(T) \left.\frac{\partial T}{\partial r}\right|_{r=R}. \tag{4}$$

Since the net heat flux to the domain is null, the axial direction, z, is homogeneous and we can apply periodic boundary conditions along the streamwise direction.

Table 1
Parameters of the simulations. Case 1: Constant fluid properties, Case 2: Low sensitivity to temperature, Case 3: Mid sensitivity to temperature and Case 4: High sensitivity to temperature.

Case	$Re_{\tau 0}$	Pr_0	$T_0/T_{\tau 0}$	Line style (Color)
1	180	0.7	$\rightarrow \infty$	Solid (Black)
2	180	0.7	1000	Long-dashed (Red)
3	180	0.7	500	Dashed–dotted (Blue)
4	180	0.7	250	Dashed (Green)

Several averages will be used throughout the paper. The brackets $\langle\cdot\rangle$ indicate mean values, averaged in time and over the homogeneous direction, z. Primed variables denote fluctuations with respect to these mean values. Bulk variables, denoted with a b sub-index, are averaged in time, over the homogeneous direction z, and over the cross-plane area $\Omega(r,\theta)$. In particular, we define the bulk velocity

$$U_b = \frac{1}{\pi R^2}\int_\Omega \langle u_z\rangle \, d\Omega, \tag{5}$$

and the bulk temperature

$$T_b = \frac{1}{\pi R^2 U_b}\int_\Omega \langle u_z T\rangle \, d\Omega, \tag{6}$$

which is a mass-flux weighted average of the temperature field.

The variation of the kinematic viscosity and the thermal diffusivity with temperature, $\nu(T)$ and $\alpha(T)$, are prescribed by the following power-laws,

$$\frac{\nu}{\nu_0} = \left(\frac{T}{T_0}\right)^{e_\nu}, \frac{\alpha}{\alpha_0} = \left(\frac{T}{T_0}\right)^{e_\alpha}, \tag{7}$$

where ν_0, α_0 and T_0 are constant reference values. The exponents $e_\nu = -3$ and $e_\alpha = 0.3$ are selected to represent the behavior of typical molten salts encountered in solar central receivers (Benoit et al., 2016).

Apart from these two exponents, the problem is governed by three non-dimensional parameters: the reference Reynolds number $Re_{\tau 0} = u_{\tau 0}R/\nu_0$, the reference Prandtl number $Pr_0 = \nu_0/\alpha_0$ and the normalized temperature $T_0/T_{\tau 0}$, where $u_{\tau 0} = \sqrt{-R\partial p/\partial z/(2\rho)}$ and $T_{\tau 0} = \overline{q}''_w/\rho C_p u_{\tau 0}$ are respectively the friction velocity and the friction temperature for the case with constant fluid properties.

Once the working fluid is selected, (i.e., the values of e_α and e_ν are given), the effect of varying fluid properties on the system is mainly determined by the ratio $T_0/T_{\tau 0}$. In the present study, the value of e_α is low, so that significant changes in thermal diffusivity are not expected. Therefore, the temperature distribution in the fluid is primarily influenced by the heat flux at the wall, which depends on the boundary conditions. The friction temperature $T_{\tau 0}$ serves as an indicator of how much the fluid's temperature varies, ΔT, due to the combined effects of heat flux and viscous dissipation near the boundary. The kinematic viscosity and thermal diffusivity of the fluid, which follow power-law relationships based on temperature (as described in Eq. (7)), change in proportion to the ratio $\Delta T/T_0$, which is on the order of $T_{\tau 0}/T_0$. If the ratio $T_0/T_{\tau 0}$ is large, the resulting changes in fluid properties are small. However, as this ratio decreases, the percentage changes in kinematic viscosity and thermal diffusivity become more significant. Note that in the case of constant fluid properties (where these properties do not vary with temperature), the ratio $T_0/T_{\tau 0}$ tends to infinity, making it irrelevant for the analysis. The ranges of variation of averaged kinematic viscosity and thermal diffusivity with temperature in the computational domain for the four cases of study are graphically shown in Fig. 1. For the most sensitive case, Case 4, the viscosity changes in the domain from ∼50% to ∼275% of the constant value, ν_0, whilst the diffusivity changes only from ∼90% to ∼107% of α_0.

The values of the governing parameters selected for the present study are provided in Table 1. All simulations are run with constant mean pressure gradient, ensuring that the $Re_{\tau 0} = 180$ for all cases. Case 1 has constant fluid properties and the remaining three cases have

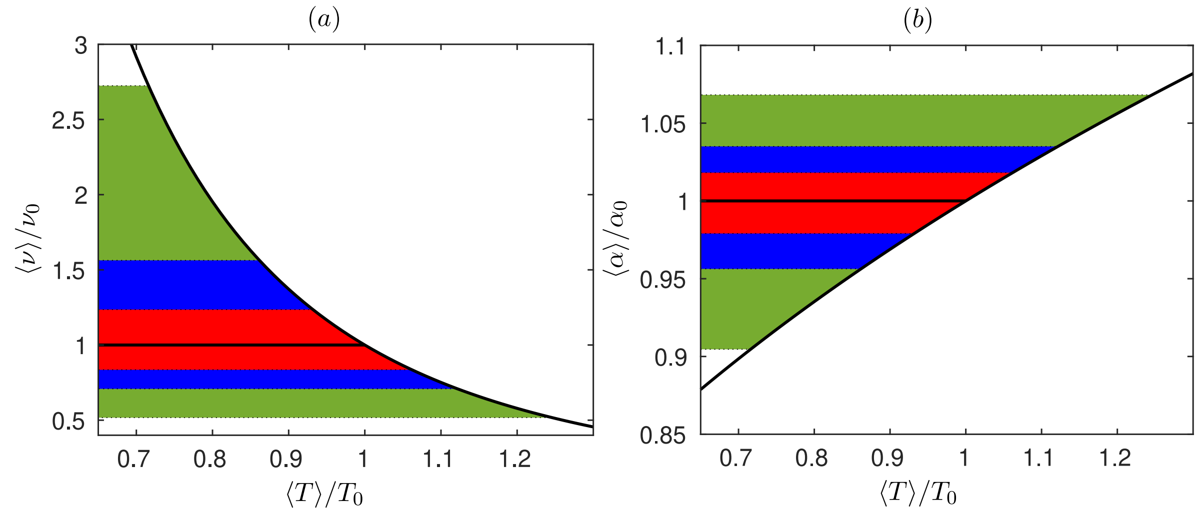

Fig. 1. Range of variation in the computational domain of kinematic viscosity (a) and thermal diffusivity (b) with temperature. Colors are as described in Table 1. (For interpretation of the references to color in this figure legend, the reader is referred to the web version of this article.)

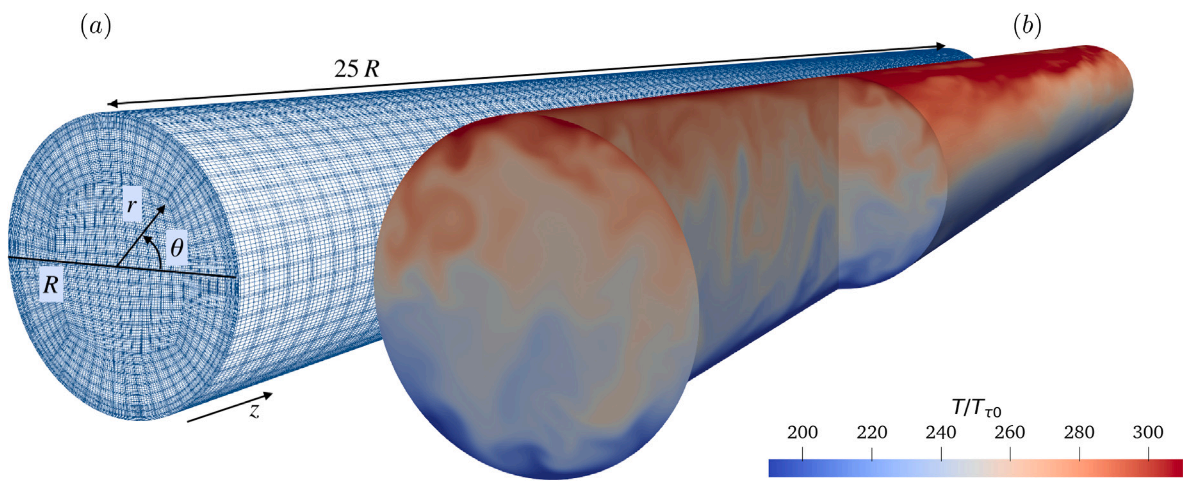

Fig. 2. Domain geometry and grid for the computational study (left) and instantaneous temperature field for Case 4 with variable fluid properties (right).

decreasing values of $T_0/T_{\tau 0}$, and consequently increasing sensitivity to variable fluid properties. For all the simulations presented here, we choose the initial mass averaged temperature to be equal to T_0. Therefore, energy conservation implies that $T_b = T_0$ throughout the computation. Note that the same is not true for ν_b and α_b, which will depart from the reference values ν_0 and α_0 due to the power law dependence of Eq. (7) with the temperature.

The simulations are performed using the code Nek5000 (Fischer et al., 2008), which uses a spectral element method, solving the incompressible Navier–Stokes equations on Gauss–Lobatto–Legendre nodes. The computational domain consists of a straight circular pipe of length $25R$, discretized with 55 440 spectral elements of polynomial order $N = 7$, with 105 elements in the stream-wise direction and 528 elements in the cross-plane (Fig. 2(a)). The first grid point in the radial direction is located at $\Delta r_{min} u_{\tau 0}/\nu_0 \simeq 0.25$ from the wall, having a maximum radial mesh size of $\Delta r_{max} u_{\tau 0}/\nu_0 \leq 3.5$. In the circumferential direction we have $\Delta (R\theta)_{max} u_{\tau 0}/\nu_0 \leq 3.5$, while in the axial direction the grid size ranges from $\Delta z_{min} u_{\tau 0}/\nu_0 \simeq 2.8$ to $\Delta z_{max} u_{\tau 0}/\nu_0 \leq 9$. This resolution is slightly better than the DNS of turbulent pipe flow (without heat transfer) carried out by El Khoury et al. (2013) also using Nek5000. The computational time step selected maintains a Courant–Friedrich–Levy number of $CFL \leq 0.5$.

3. Results and discussion

The statistics for the different cases were accumulated for a time interval, given in terms of eddy turnover times, of $t_{tot} = 312R/u_{\tau 0}$, which is roughly equal to 180 wash-out times. The statistical convergence of the mean bulk velocity was assessed using the block averaging method, revealing that the standard deviation of sub-interval means relative to the overall mean was less than 1%. Note that the averaging interval exceeds the one reported by Pirozzoli et al. (2021), which was 204 eddy-turnover times for an adiabatic pipe flow at $Re_\tau = 180.3$. However, the fact that the flow is not statistically homogeneous along the circumferential direction implies that significantly longer integration times would be required to obtain better statistical convergence. No advantage was taken from the mirror symmetry of the problem, so that the asymmetry in some of the plots below provides a measure of the convergence of the statistics. For illustration, Fig. 2(b) shows a snapshot of the instantaneous temperature distribution $T/T_{\tau 0}$ along the pipe for Case 4.

3.1. Circumferential distributions on the pipe wall

The circumferential distribution of temperature on the pipe wall is presented in Fig. 3(a) for the three cases as the change from their corresponding bulk temperatures, $(\langle T_w \rangle - T_b)/T_{\tau 0}$. The case with constant

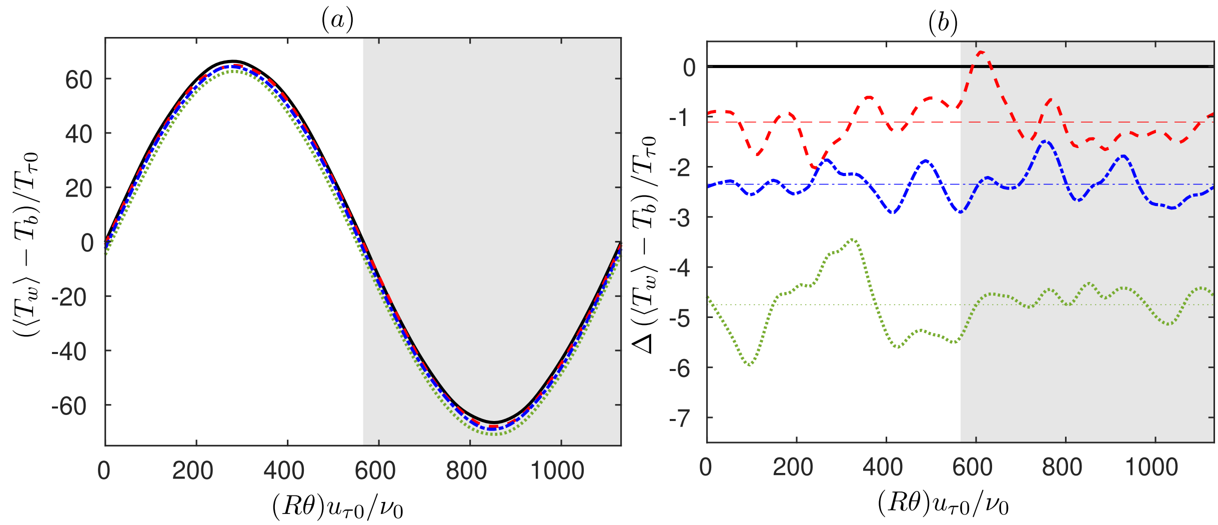

Fig. 3. Circumferential variation of wall temperature minus bulk temperature at pipe wall (*a*) and increment from Case 1 (*b*). Shaded area indicates cooled half of the pipe. Lines are as described in Table 1. Thinner lines present circumferentially averaged values.

properties, Case 1, shows an anti-symmetrical temperature distribution with peak amplitude $(\langle T_w \rangle - T_b)/T_{\tau 0} \sim 65$. When $T_0/T_{\tau 0}$ decreases and ν and α are allowed to vary, Fig. 3(*a*) shows that the wall temperature shifts to lower temperatures. This shift is characterized in Fig. 3(*b*) by the difference in wall-temperature between the cases with variable properties (Cases 2, 3 and 4) and the case with constant properties (Case 1), $\Delta(\langle T \rangle_w - T_b)_i/T_{\tau 0}$, where

$$\Delta(\xi)_i = [\xi]_{case\ i} - [\xi]_{case\ 1} \tag{8}$$

$i = 2, 3$ and 4. The oscillations we see in this variable are likely an effect attributable to lack of convergence of the statistics. The circumferential average of the normalized temperature difference shows that $(\langle T_w \rangle - T_b)/T_{\tau 0}$ for Case 2 is shifted by ~ -1.1 and Case 3 by ~ -2.4, while Case 4 presents a shift of about ~ -4.7.

The non-uniform temperature distribution produces a variation of the fluid properties, viscosity and diffusivity, leading to a non-homogeneous distribution of shear stress, $\langle \tau_w \rangle$, at the wall and hence, of the local friction velocity $u_\tau(\theta) = \sqrt{\langle \tau_w \rangle/\rho}$. The variation of the friction velocity with the circumferential position is provided in Fig. 4(*a*). For the most sensitive case, Case 4, the friction velocity varies about $\sim$−12% with respect to Case 1 in the heated part, and about $\sim +14\%$ in the cooled part. For Case 3, the friction velocity varies fairly symmetrically from −6% to +6%, while the change in u_τ for Case 2 is only ±2.5%. As a consequence, the local friction coefficient $C_f = 2u_\tau^2/U_b^2$ roughly changes $52\%, 25\%$ and 10% from top to bottom for Cases 4, 3 and 2 respectively.

The local friction temperature, $T_\tau(\theta)$, defined as $q''_w(\theta) = \rho C_p u_\tau T_\tau$, is shown in Fig. 4(*b*). The percent variation of the friction temperature from the case with constant fluid properties is equal and of opposite sign to the variation of $u_\tau/u_{\tau 0}$, since the thermal boundary condition implies $u_\tau(\theta)T_\tau(\theta) = u_{\tau 0}T_{\tau 0}\pi \sin\theta$ for all cases.

Circumferential variations of the wall values of kinematic viscosity, $\langle \nu \rangle_w$, and the thermal diffusivity, $\langle \alpha \rangle_w$, together with the local friction velocity, u_τ, result in non-homogeneous profiles for the local friction Reynolds number ($Re_{\tau,w} = u_\tau R/\langle \nu \rangle_w$) and local Prandtl number ($Pr_w = \langle \nu \rangle_w/\langle \alpha \rangle_w$), which are plotted in Fig. 5. Changes are significant. The Reynolds number varies a 33% from the hot to the cold side of the pipe in Case 2, a 66% in Case 3 and a 129% in Case 4, ranging from $Re_{\tau,w} \sim 78$ to $Re_{\tau,w} \sim 310$ in the latter. Prandtl number changes from $Pr_w \sim 0.33$ to $Pr_w \sim 2.13$ in the most sensitive case, which means a 257% variation from the hot and cold sides of the pipe. This figure is reduced to 96% for Case 3 and to 43% for Case 2. Finally, the local Péclet number, $Pe_{\tau,w} = Re_{\tau,w}Pr_w$, is reported in Fig. 5(*c*). It takes a value of about $Pe_{\tau,w} \sim 105$ at the hot side of the pipe, and about $Pe_{\tau,w} \sim 159$ at the cold side for Case 4, when $Pe_{\tau,w} \sim 126$ for Case 1. As expected, the variation in the local Péclet number for Cases 3 and 2 is smaller, roughly 115 to 140 and 120 to 132, respectively, from hot to cold sides of the pipe. Note that, while the local Reynolds number is increased (decreased) in the hot (cold) side of the pipe, the local Péclet number is decreased (increased). This suggests that, when the thermal boundary layers get thicker, the momentum boundary layers get thinner (and vice-versa).

Unlike cases with iso-thermal or mixed boundary conditions (Piller, 2005), a constant heat flux boundary condition permits temperature fluctuations at the wall. Fig. 6 shows the circumferential variation of the RMS temperature fluctuations on the wall for the four cases of study. Values range from $T'_{rms}/T_{\tau 0} \sim 5.5$ to 7.8 and have local maximums in the regions where the heat flux, positive or negative, is more intense, $\theta = \pi/2$ and $\theta = 3\pi/2$. These fluctuations are found to be largely influenced by the variable fluid properties. As $T_0/T_{\tau 0}$ decrease, the fluctuations at the heated side are mitigated, while they are exacerbated at the cooled side. For Case 4, we have a $\sim +13\%$ increment in the $T'_{rms}/T_{\tau 0}$ peak at the cold bottom compared to the case of constant fluid properties, while fluctuations are reduced by $\sim -15\%$ at the hot top.

3.2. Cross-plane flow distributions

The variation of the flow properties in the cross-plane are shown through the use of contour plots in Figs. 7–10, where the left half of the pipe corresponds to the case with constant properties (Case 1) and the right half belongs to the more sensitive case (Case 4), facilitating the comparison between the two cases. Since the heat flux takes a top to bottom direction and the peak temperatures are reached at $\theta = \pi/2$ and $\theta = 3\pi/2$, the profiles shown in the figures below correspond to a cut through the symmetry axis, $x = 0$, because this is the location where differences are more apparent.

The results for the mean axial velocity are provided in Fig. 7, with Fig. 7(*a*) showing the contour plots comparison and Fig. 7(*b*) plotting the mean axial velocity profiles for all the cases. Fig. 7(*c*) gives the variations of $\langle u_z \rangle$ with respect to Case 1, namely $\Delta(\langle u_z \rangle)_i/u_{\tau 0}, i = 2, 3, 4$. The mean axial velocity profiles tend to lose their symmetry when $T_0/T_{\tau 0}$ decreases. The velocity gradient becomes smaller near the cold half of the pipe, with a thicker boundary layer caused by the increased viscosity. The opposite is true for the heated half of the pipe, where the mean velocity profile shows a thinner boundary layer and a steeper

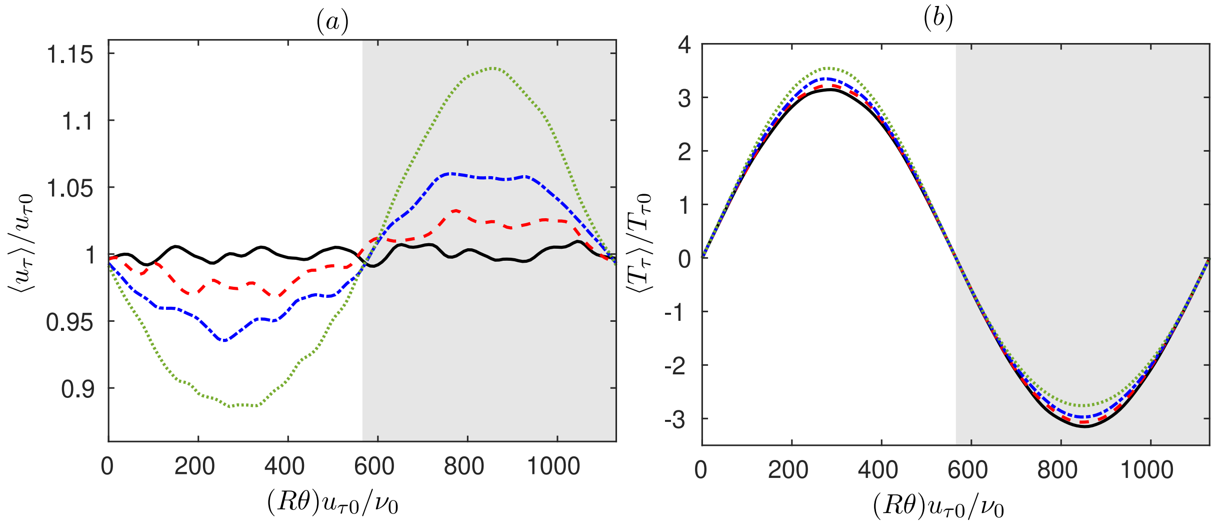

Fig. 4. Circumferential variation of local friction velocity (*a*) and local friction temperature (*b*) at pipe wall. Shaded area indicates cooled half of the pipe. Lines are as described in Table 1.

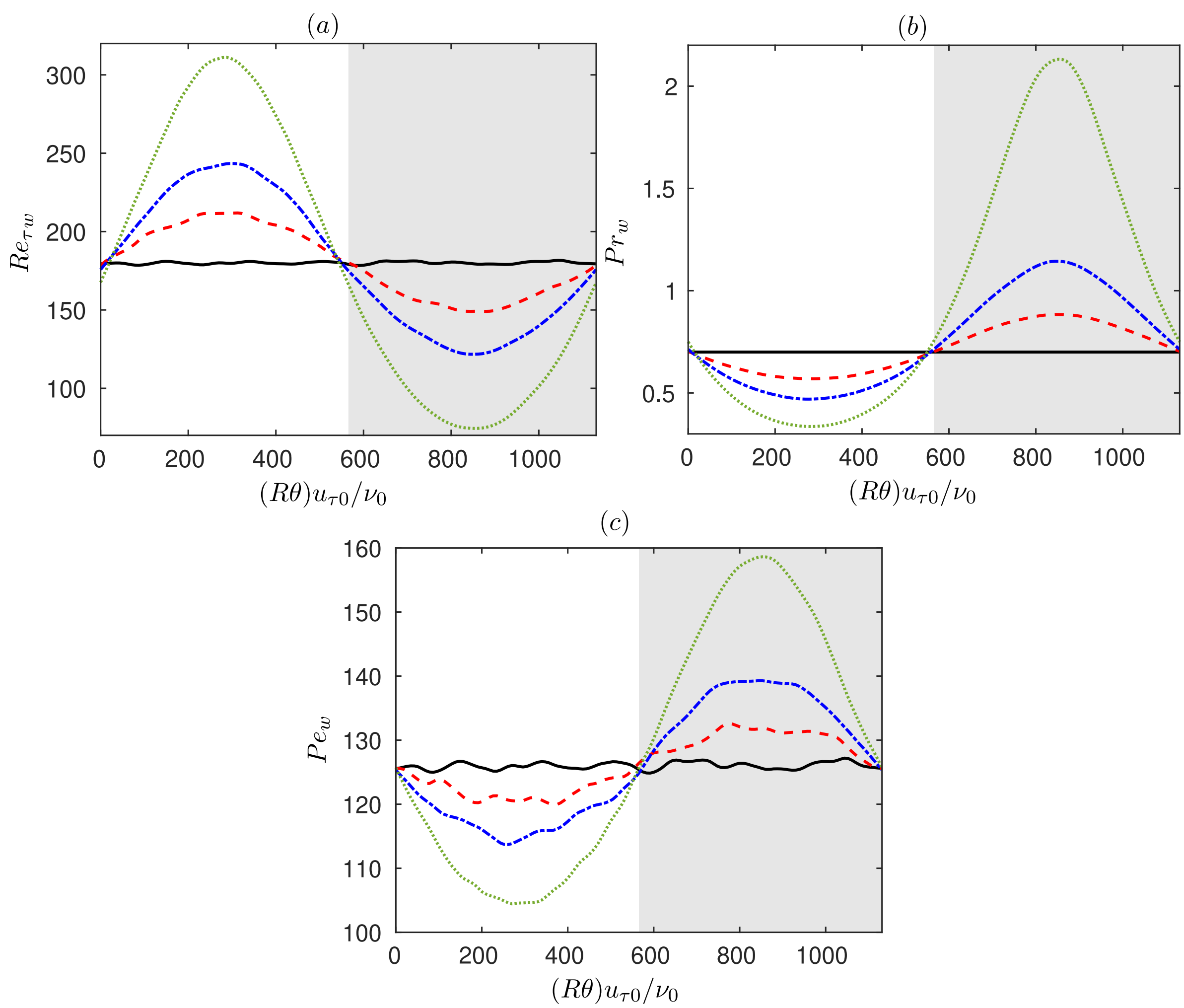

Fig. 5. Circumferential variation of local friction Reynolds number (*a*), local Prandtl number (*b*) and local Péclet number (*c*) at pipe wall. Shaded area indicates cooled half of the pipe. Lines are as described in Table 1.

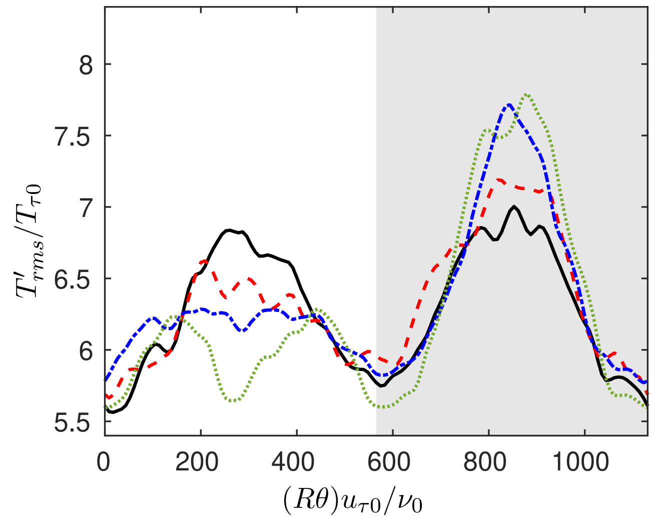

Fig. 6. Circumferential variation of local RMS temperature fluctuation on the pipe wall. Shaded area indicates cooled half of the pipe. Lines are as described in Table 1.

gradient at the wall for the cases with temperature dependent fluid properties. For the most sensitive case (Case 4), the axial flow velocity is reduced by $\sim -3u_{\tau 0}$ near the cooled wall, by $\sim -0.7u_{\tau 0}$ at mid channel but increased $\sim +2u_{\tau 0}$ near the heated wall.

The turbulent kinetic energy (TKE) contours and profiles are compared in Fig. 8. We observe that the peak TKE is enhanced near the cold bottom, where the mean velocity gradient is reduced, while the opposite occurs in the hot side. Note also that the position of the peak TKE moves closer to the pipe wall as the mean velocity gradient increases. While the latter is the expected behavior in incompressible wall-turbulent flows, the increased TKE for the reduced velocity gradients are not. However, this behavior is consistent with previous observations (Zonta et al., 2012; Lee et al., 2013).

The profile of the difference between the mean temperature and the bulk temperature, normalized with the global friction temperature, $(\langle T\rangle - T_b)/T_{\tau 0}$, is shown in Fig. 9. The temperature distribution in the cross-plane is dominated by the heat flux boundary condition on the wall. Highest mean temperature is reached at the top where the heat flux is maximum and lowest mean temperature is found at the bottom where the heat flux is more negative. Although the profiles for the four cases are similar, the local variation in Prandtl number produces an effect on the thermal boundary layers near the pipe wall. Fig. 9(c) provides with the temperature increment in Cases 2, 3 and 4 with respect to the temperature obtained for Case 1. We distinguish a central region where the temperature changes linearly from top to bottom with equal slope for the three cases, with Case 2 being shifted towards higher normalized temperatures by $\sim +0.7$, Case 3 by $\sim +1.7$ and Case 4 by $\sim +3.5$. Close to the wall the behavior is different and the cases with variable properties have lower temperatures, consistent with the discussion of the temperature profile on the wall (Fig. 3).

Fig. 10 reports the RMS temperature fluctuations in the cross-plane and on the vertical diameter of the pipe. Near the walls, the behavior of the temperature RMS is qualitatively similar to the behavior of the TKE. Fluctuations are promoted near the cooled wall, but damped near the heated wall. Note that these tendencies are now consistent with the changes in the mean temperature gradients. For the most sensitive case, Case 4, there is a +8.8% increment in the peak of $T'_{rms}/T_{\tau 0}$ at the cooled part of the pipe wall, whilst the peak of $T'_{rms}/T_{\tau 0}$ decreases −13.8% at the heated wall.

3.3. Secondary flows and heat fluxes

The introduction of variable fluid properties in the computation leads to the existence of small, but discernible, mean velocities in the radial and circumferential directions, caused by the variations in temperature in the cross-plane. Fig. 11 shows the direction $(\langle u_x\rangle, \langle u_y\rangle)$ and magnitude ($u_{sec} = \sqrt{\langle u_x\rangle^2 + \langle u_y\rangle^2}$) of these secondary flows, for all three cases. For Case 4, the secondary vectors are of order $O(u_{sec}/u_{\tau 0}) \sim 0.1$, with a maximum of $u_{sec_{max}} = 0.169u_{\tau 0}$, which accounts for ∼1.2% of the bulk velocity. Note that the intensity of the secondary flow of Case 4 is comparable to that of the secondary flows in square ducts at comparable Re_τ (Pinelli et al., 2010; Pirozzoli et al., 2018).

The presence of secondary flows are associated with the existence of non-zero stream-wise vorticity, which appears superimposed in Fig. 11 as colored contours in the range $-2.2 \le \langle\omega_z\rangle R/u_{\tau 0} \le 2.2$. In order to have a better understanding on the nature of these secondary flows, we analyze the different terms in the stream-wise vorticity equation. The equation for the vorticity vector reads as in Eq. (9).

$$\frac{\partial\vec{\omega}}{\partial t} + (\vec{u}\cdot\nabla)\,\vec{\omega} = (\vec{\omega}\cdot\nabla)\,\vec{u} + \frac{1}{\rho}\left[\nabla\times\left(\nabla\cdot\vec{\vec{\tau}}\right)\right] \tag{9}$$

Considering that our problem is homogeneous in t and z, and that $\nabla\cdot\vec{u} = 0$ and $\nabla\cdot\vec{\omega} = 0$, and projecting in the axial direction, the equation of the averaged stream-wise vorticity leads to

$$\begin{aligned}&\overbrace{\langle u_x\rangle\partial_x\langle\omega_z\rangle + \langle u_y\rangle\partial_y\langle\omega_z\rangle}^{\text{advection term}} + \overbrace{\left(\partial_{xx} - \partial_{yy}\right)\langle u'_x u'_y\rangle + \partial_{xy}\left(\langle {u'_y}^2\rangle - \langle {u'_x}^2\rangle\right)}^{\text{turbulent production term}}\\ &= \underbrace{\langle\nu\rangle\left(\partial_{xx} + \partial_{yy}\right)\langle\omega_z\rangle}_{\text{mean dissipation term}}\\ &+ \underbrace{\langle\nu'\left(\partial_{xx} + \partial_{yy}\right)\omega'_z\rangle + \langle\left(\partial_x u_y + \partial_y u_x\right)\left(\partial_{xx} - \partial_{yy}\right)\nu\rangle + 2\langle\left(\partial_y u_y - \partial_x u_x\right)\partial_{xy}\nu\rangle}_{\text{variable viscosity term}}\end{aligned} \tag{10}$$

We have identified four terms contributing to the change in stream-wise vorticity. The first term in Eq. (10) is the convection of ω_z by the cross-flow velocities. The second term is the production of ω_z by the Reynolds stresses (with negative sign). The third term is the dissipation created by the mean viscosity $\langle\nu\rangle$. Finally, the fourth term is the contribution due to the viscosity gradients and fluctuations. Note that this last term would not exist in the case of constant fluid properties.

The magnitude of these terms are evaluated for Case 4 in a 10-degrees sector, centered in $y = 0$. Values reported in Fig. 12 are circumferentially averaged and adequately symmetrized to reduce the noise in the results. Figures correspond to non-dimensional values using R as the reference distance, $u_{\tau 0}$ as the reference velocity and ν_0 as the reference viscosity. As shown in Fig. 12, the streamwise vorticity and all the terms are null near the axis of the pipe. When we approach the wall, $\langle\omega_z\rangle$ starts increasing at $r/R \sim 0.6$ ($(1-r)u_{\tau 0}/\nu_0 \sim 70$), getting a local maximum at $r/R \sim 0.8$ ($(1-r)u_{\tau 0}/\nu_0 \sim 36$). Closer to the wall, at $r/R \sim 0.9$ ($(1-r)u_{\tau 0}/\nu_0 \sim 20$), the streamwise vorticity becomes negative, reaching the minimum at the wall. Focusing now on the contribution from the different terms in Eq. (10), it is apparent that the existence of ω_z is mainly driven by the difference in Reynolds stresses near the walls, indicating that this secondary flow is of the second kind, following the classification by Prandtl (1926). The analysis shows that the turbulent stresses gradients are approximately balanced by the mean diffusion term, with the advection term having a much smaller contribution. This happens in almost all the domain, except for distances $(1-r)u_{\tau 0}/\nu_0 \le 5$. Closer to the wall, the turbulent stresses contribution vanishes and the term gathering the effect of the viscosity fluctuations and gradients becomes increasingly important.

These secondary flows, despite their small magnitude, have an important practical contribution to the heat fluxes in the cross-plane. We can distinguish, more clearly in Case 4, two anti-symmetrical vortex moving hotter fluid from top to bottom along the vertical diameter and returning colder fluid along the pipe walls, see Fig. 11c. In order to assess the influence of the secondary flows in the heat fluxes, let consider the transport equation for the mean energy in Cartesian

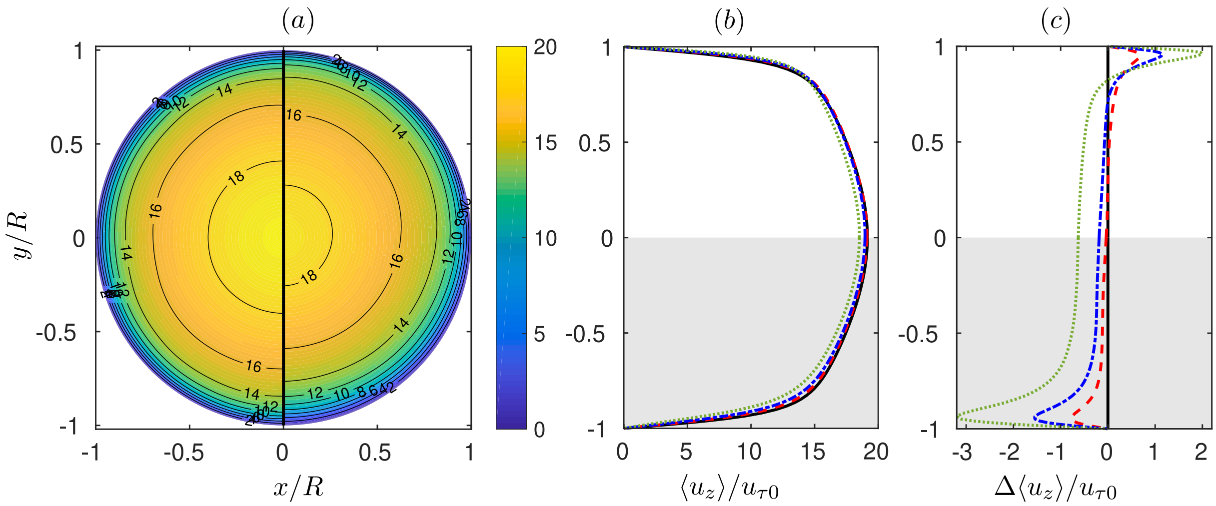

Fig. 7. Mean axial velocity $(\langle u_z \rangle / u_{\tau 0})$ comparison. (*a*) Case 1 field (left) is compared with Case 4 field (right). (*b*) Top-bottom profile comparison. (*c*) Variations with respect to Case 1, $\Delta\langle u_z \rangle / u_{\tau 0}$. Shaded area indicates cooled half of the pipe. Lines are as described in Table 1.

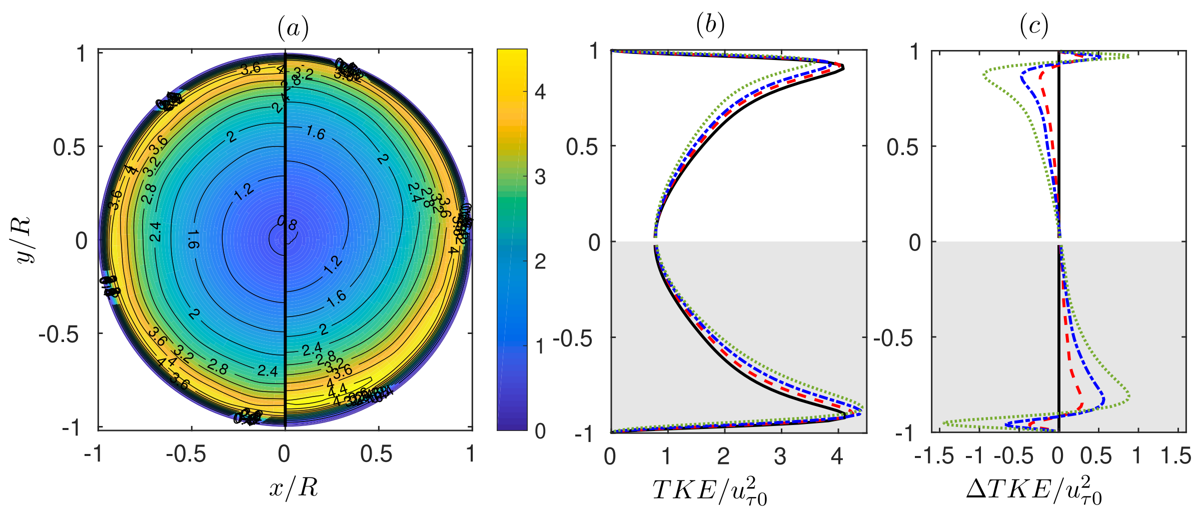

Fig. 8. Turbulent kinetic energy profiles, $TKE = 1/2\langle u'^2 + v'^2 + w'^2 \rangle / u_{\tau 0}^2$. (*a*) Case 1 field (left) is compared with Case 4 field (right). (*b*) Top-bottom profile comparison. (*c*) Variations with respect to Case 1, $\Delta TKE/u_{\tau 0}^2$. Shaded area indicates cooled half of the pipe. Lines are as described in Table 1.

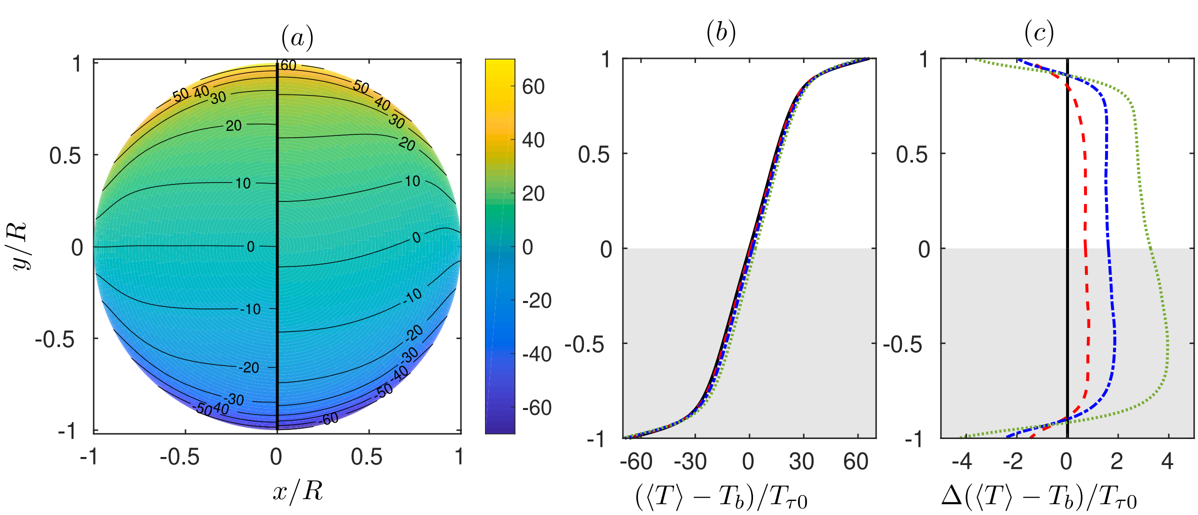

Fig. 9. Mean temperature $(\langle T \rangle - T_b)/T_{\tau 0}$ comparison. (*a*) Case 1 field (left) is compared with Case 3 field (right). (*b*) Top-bottom profile comparison. (*c*) Mean temperature increment from Case 1 $\Delta(\langle T \rangle - T_b)/T_{\tau 0}$. Shaded area indicates cooled half of the pipe. Lines are as described in Table 1.

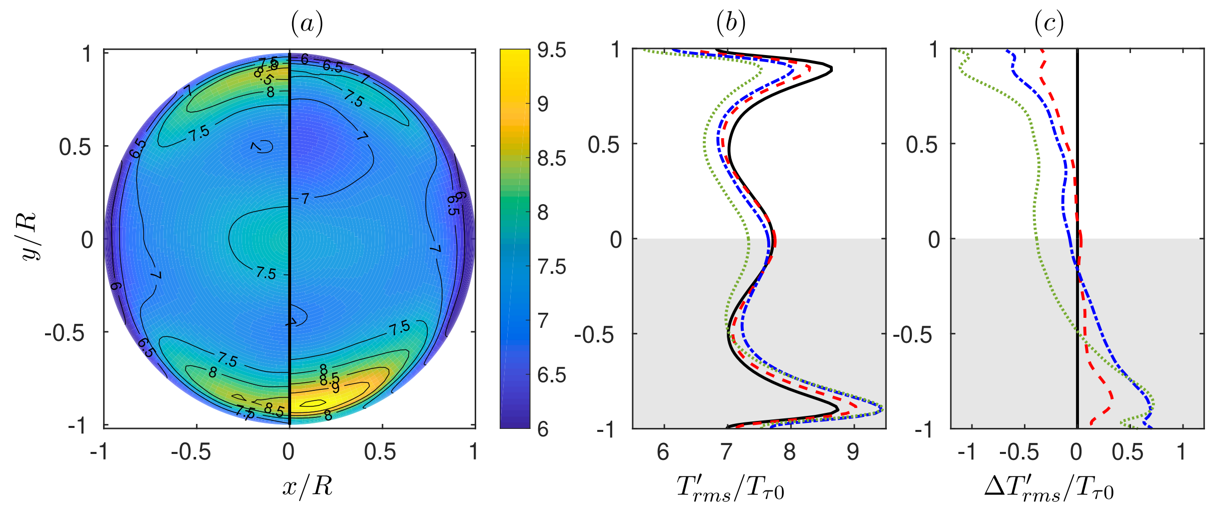

Fig. 10. Root mean square temperature fluctuation $\left(T'_{rms}/T_{\tau0}\right)$ comparison. (*a*) Case 1 field (left) is compared with Case 3 field (right). (*b*) Top-bottom profile comparison. (*c*) Mean temperature increment from Case 1 $\Delta T'_{rms}/T_{\tau0}$. Shaded area indicates cooled half of the pipe. Lines are as described in Table 1.

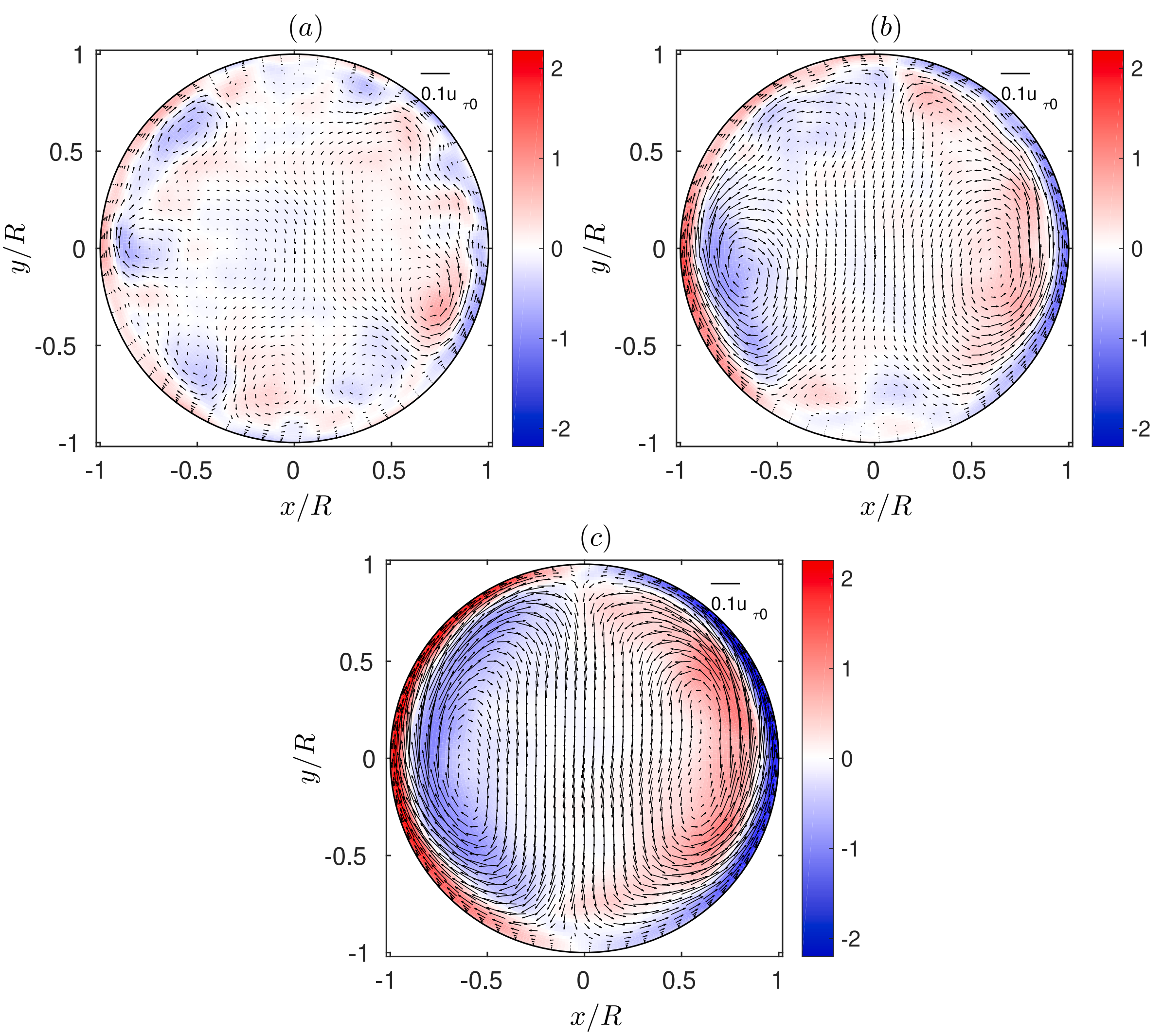

Fig. 11. Secondary velocity vectors, u_sec and streamwise vorticity, $\langle\omega_z\rangle R/u_{\tau0}$, contours. (*a*) Case 2. (*b*) Case 3. (*c*) Case 4. (For interpretation of the references to color in this figure legend, the reader is referred to the web version of this article.)

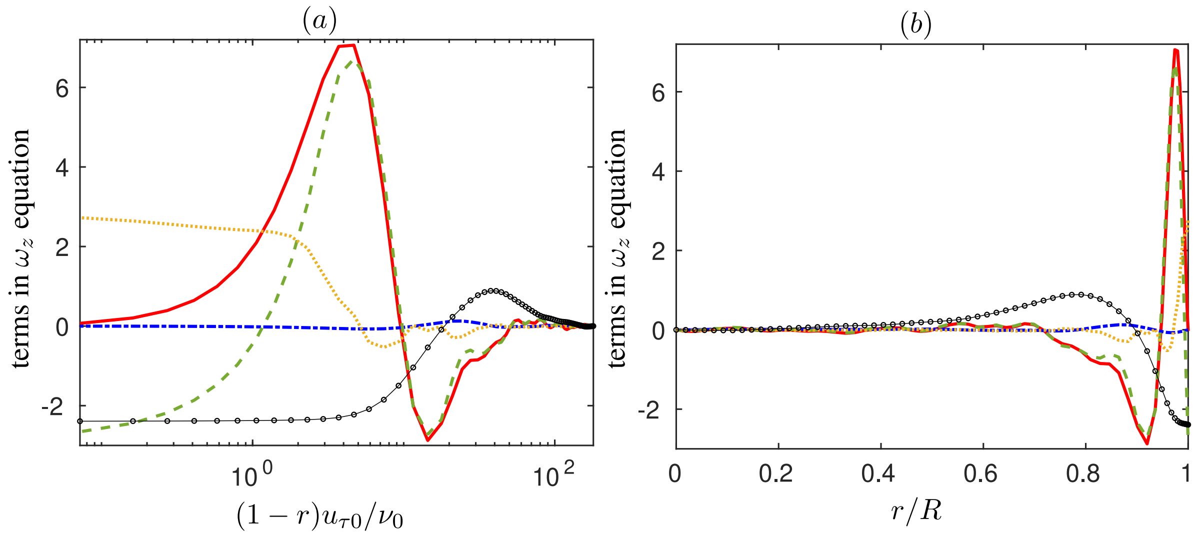

Fig. 12. Streamwise vorticity equation terms analysis for Case 4. Blue dash-dotted line: mean advection term; red solid line: turbulent stresses term; green dashed line: mean diffusion term; yellow dotted line: variable viscosity term; black symbols: $\langle\omega_z\rangle R/u_{\tau 0}$. (For interpretation of the references to color in this figure legend, the reader is referred to the web version of this article.)

coordinates:

$$\frac{\partial\langle u_i T\rangle}{\partial x_i} = \frac{\partial}{\partial x_i}\left(\left\langle \alpha(T)\frac{\partial T}{\partial x_i}\right\rangle\right). \tag{11}$$

From this equation, we can define the total heat flux vector, $\vec{\Phi}$, as

$$\Phi_i = \langle u_i\rangle(\langle T\rangle - T_b) + \langle u_i' T'\rangle - \langle\alpha(T)\rangle\langle\frac{\partial T}{\partial x_i}\rangle. \tag{12}$$

where we have added, with negative sign, the contribution of the solenoidal component of the flux $\langle u_i\rangle T_b$ and we have neglected the term $\langle\alpha'\partial x_i T'\rangle$ (note that $T'/T_0 \ll 1$, and then $\alpha'/\alpha_0 \ll 1$).

In Fig. 13 we show the three terms of the vertical component of total heat flux vector, Φ_y: the secondary flow heat flux, $\langle u_y\rangle(\langle T\rangle - T_b)$, the turbulent heat flux, $\langle u_y' T'\rangle$, and the diffusive heat flux, $-\langle\alpha\rangle\partial\langle T\rangle/\partial y$, normalized with $u_{\tau 0}T_{\tau 0}$, for all 4 cases. Heat flux distributions are provided on two horizontal planes, at $y/R = +0.5$ within the heated upper part and at $y/R = -0.5$ within the cooled lower part. The sign criteria we follow is that negative values indicate heat flux going from top to bottom.

As shown in Fig. 13, the normalized turbulent heat fluxes $\langle u_y' T'\rangle/(u_{\tau 0}T_{\tau 0})$ are dominant in most of the flow domain. Starting from zero on the pipe surface, the profiles reach a minimum near the wall and then increase slightly towards the symmetry axis, $x = 0$. Regarding the heat flux produced by the secondary flows, $\langle u_y\rangle(\langle T\rangle - T_b)/(u_{\tau 0}T_{\tau 0})$, we observe an increasing contribution with the fluid variables sensitivity to temperature. Near the walls, the secondary heat fluxes are strong and positive, at $y/R = +0.5$, or negative, at $y/R = -0.5$, indicating a flow stream moving upwards, transporting fluid with mean temperature above or below T_b respectively. Near the symmetry axis, the flows moves from top to bottom, creating secondary fluxes of the opposite sign. For Case 4, the contribution of these fluxes is even larger than that of the diffusive terms, accounting for up to one third of the total heat flux crossing the pipe. Note that the heat flux contribution of the secondary flows should be zero for Case 1 and that deviations from zero gives an indication of the statistics error due to lack of convergence.

3.4. Mean flow properties

Integral quantities are of great importance for engineering purposes in general and, in particular, for the design of Solar Power Towers, where their economic perspectives heavily depend on the working fluid performance. In this section, we quantify the performance output from the computation in terms of the mass flow rate, the friction coefficient and the heat transfer coefficient.

Table 2
Mean pipe mass flow and friction coefficient.

Case	$Re_{\tau 0}$	Re_b	$U_b/u_{\tau 0}$	$C_f \cdot 10^{-3}$
Case 1	180.0	5262	14.59	9.36
Case 2	180.0	5244	14.56	9.43
Case 3	180.0	5188	14.41	9.63
Case 4	180.0	5039	14.00	10.21
El Khoury et al. (2013)	182.2	5300	14.54	9.45
Wu and Moin (2008)	181.4	5300	14.61	9.37
Redjem-Saad et al. (2007)	187.0	5500	14.70	9.25
Piller (2005)	180.0	5273	14.65	9.32
Eggels et al. (1994)	179.9	5300	14.73	9.22
Colebrook formula		5300		9.21

Table 2 presents the results for the mass flow, in terms of the bulk velocity, $U_b/u_{\tau 0}$, and the friction coefficient, C_f, predicted in our computations. Results are compared with those obtained from previous reported DNS with constant properties and with the Colebrook's empirical formula, showing good agreement with Case 1. Regarding the cases with variable fluid properties, as the parameter $T_0/T_{\tau 0}$ is decreased, we see an increment of the overall flow resistance, that implies a +9.1% in the friction coefficient for Case 4, a +2.9% for Case 3 and a +0.8% for Case 2. The reasons for this increase in the friction coefficient are probably related to two separate contributions, namely the need to sustain secondary motions and an overall increase of the fluid viscosity. The latter is apparent in Fig. 1(a), showing that the viscosity distribution is clearly skewed towards $\nu/\nu_0 > 1$.

Regarding the thermal performance, we quantify the overall impact on heat transfer defining integral values for the Nusselt number on the heated surface and on the cooled surface as

$$Nu^H = \frac{2R\pi}{\rho C_p \int_0^\pi \langle\alpha_w\rangle d\theta}\,\frac{\int_0^\pi q_w'' d\theta}{\int_0^\pi (\langle T_w\rangle - T_b) d\theta} \tag{13}$$

$$Nu^C = \frac{2R\pi}{\rho C_p \int_\pi^{2\pi} \langle\alpha_w\rangle d\theta}\,\frac{\int_\pi^{2\pi} q_w'' d\theta}{\int_\pi^{2\pi} (\langle T_w\rangle - T_b) d\theta}. \tag{14}$$

Table 3 quantifies the heat transfer in terms of the integral Nusselt numbers (Nu) for all the cases. Reynolds and Prandtl numbers provided are also average values obtained integrating the local surface values on the hot region ($\theta = 0$ to π) and on the cold region ($\theta = \pi$ to 2π). Note that for the case with constant fluid properties (Case 1), the Nusselt, Reynolds and Prandtl numbers averaged over the hot and cold regions are the same, and hence only one value is reported in Table 3. The value

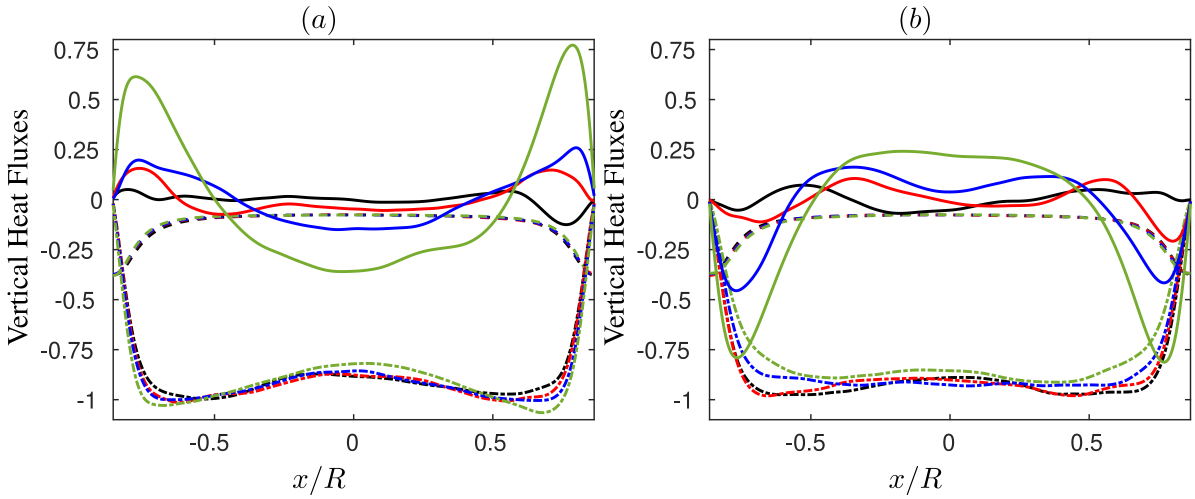

Fig. 13. Vertical heat fluxes for all cases at plane $y/R = +0.5$ (a) and at plane $y/R = -0.5$ (b). Colors correspond to case assignment in Table 1. Solid lines: secondary flow heat fluxes, $\langle u_y\rangle(\langle T\rangle - T_b)/u_{\tau 0}T_{\tau 0}$, dash-dotted lines: turbulent heat fluxes, $\langle u_y'T'\rangle/u_{\tau 0}T_{\tau 0}$, and dashed lines: diffusive heat fluxes, $-\langle\alpha\rangle\partial_y\langle T\rangle/u_{\tau 0}T_{\tau 0}$. (For interpretation of the references to color in this figure legend, the reader is referred to the web version of this article.)

Table 3
Mean Nusselt number on pipe wall.

Case	$Re_{\tau,w}$	Re_b	Pr_w	Nu
Case 1	180.0	5262	0.700	11.94
Case 2 (Hot)	199.6	5244	0.613	12.11
Case 2 (Cold)	160.4	5244	0.810	11.82
Case 3 (Hot)	218.1	5188	0.543	12.35
Case 3 (Cold)	141.6	5188	0.951	11.66
Case 4 (Hot)	253.3	5039	0.441	12.93
Case 4 (Cold)	105.2	5039	1.381	11.48
Gärtner et al. (1974)		5300	0.700	10.49
Reynolds (1963)		5300	0.700	9.85
Gnielinski formula		5300	0.700	17.51

of the Nusselt number for the case with uniform heating obtained from the Gnielinski formula is provided as reference. More appropriate is the comparison with the cases with sinusoidal heat flux boundary condition of Reynolds (1963) and Gärtner et al. (1974). Both authors calculated the turbulent heat transfer in a pipe subjected to circumferentially-varying heat flux conditions with constant fluid properties using RANS models. While Reynolds (1963) used an isotropic model for the thermal eddy-diffusivity, Gärtner et al. (1974) improved the calculations by employing a non-isotropic model. The discrepancies we found in the computed Nusselt number for Case 1, and the value obtained using the data from Reynolds (1963) or Gärtner et al. (1974), could be attributed to the simplifications applied by these authors in the radial distributions of the eddy viscosity and eddy diffusivities, and in the ratio used for the circumferential and radial diffusivities, which do not reflect the physical behavior, specially at low Reynolds numbers, as concluded in Antoranz et al. (2015). Note that the improved model of Gärtner et al. (1974) get closer to the current results (with an error of $\sim -12\%$), than the estimation of Reynolds (1963) (error of $\sim -18\%$).

The consideration of variable fluid properties in the computation produces significant differences in the local Nusselt number of the heated surface compared with the cooled surface. In the most sensitive case, Case 4, we appreciate an increment of +8.3% in Nu on the hot wall compared to the Case 1, but a reduction of −3.8% on the cold wall. In average, the overall Nusselt number increases +0.21% for Case 2, +0.54% for Case 3, and +2.22% for Case 4.

4. Conclusions

DNS of a fully-developed turbulent flow in a pipe, with circumferentially-varying heat flux boundary conditions and with temperature-dependent fluid properties, has been conducted aiming to study their effect on the turbulent heat transfer on the pipes of a Solar Heat Receiver. The analysis has been carried out for a pipe with reference friction Reynolds number $Re_{\tau 0} = 180$, reference Prandtl number $Pr_0 = 0.7$ and for four cases with different bulk temperatures, $T_0/T_{\tau 0} = \infty$, 1000, 500 and 250, corresponding with null, low, medium and high viscosity and diffusivity sensitivity to flow temperature variations.

Inasmuch as the heat flux boundary condition is the same for all cases, the mean temperature distribution on the pipe wall does not change significantly. However, the viscosity and diffusivity dependency on temperature produce the turbulent velocities and temperature fluctuations being enhanced near the cold bottom but damped near the hot top. The RMS temperature fluctuations at the pipe wall, $(T'_{rms})_w$, has increments of around +13% and reductions of around −15% for the most sensitivity case. The near wall peak of TKE has increased by +7.8% at the cold end and reduced by −14.2% at the hot end.

The non-homogeneous fluid properties induce the occurrence of secondary flows on the pipe cross-plane. We have found that although the secondary velocities are low, they have a significant impact in the vertical heat flux, accounting for one third of the total heat flux in the most sensitive case.

Finally, the analysis of the integral flow quantities has shown that, when we reduce the bulk temperature and the fluid properties are more sensitive to temperature variations, the overall friction coefficient increases by up to +9.1%. Regarding the heat transfer on the wall, characterized by the Nusselt number, we have found increasing differences from heated to cooled walls, but that means only a moderate overall increase of +2.2% in heat transfer for Case 4.

CRediT authorship contribution statement

A. Antoranz: Writing – original draft, Visualization, Validation, Investigation, Formal analysis, Data curation. **O. Flores:** Writing – review & editing, Supervision, Methodology, Conceptualization. **M. García-Villalba:** Writing – review & editing, Supervision, Methodology, Conceptualization.

Declaration of competing interest

The authors declare that they have no known competing financial interests or personal relationships that could have appeared to influence the work reported in this paper.

Acknowledgments

The authors acknowledge TU Wien Bibliothek for financial support through its Open Access Funding Programme.

Data availability

Data will be made available on request.

References

Antoranz, A., Flores, O., García-Villalba, M., 2020. DNS of turbulent pipe flow with temperature-dependent fluid properties subject to non-uniform external heating. In: Direct and Large Eddy Simulation XII. Springer, pp. 233–238.

Antoranz, A., Gonzalo, A., Flores, O., Garcia-Villalba, M., 2015. Numerical simulation of heat transfer in a pipe with non-homogeneous thermal boundary conditions. Int. J. Heat Fluid Flow 55, 45–51.

Antoranz, A., Ianiro, A., Flores, O., García-Villalba, M., 2018. Extended proper orthogonal decomposition of non-homogeneous thermal fields in a turbulent pipe flow. Int. J. Heat Mass Transfer 118, 1264–1275.

Benoit, H., Spreafico, L., Gauthier, D., Flamant, G., 2016. Review of heat transfer fluids in tube-receivers used in concentrating solar thermal systems: Properties and heat transfer coefficients. Renew. Sustain. Energy Rev. 55, 298–315.

Black, A., Sparrow, E., 1967. Experiments on turbulent heat transfer in a tube with circumferentially varying thermal boundary conditions. J. Heat Transf. 89 (3), 258–268.

Dachwitz, A., Bauer, C., Wagner, C., 2023. Streaky structures in a sinusoidally-tempered vertical turbulent pipe flow. In: 10th Int. Symp. Turbulence Heat Mass Transfer. THMT-23.

Eggels, J., Unger, F., Weiss, M., Westerweel, J., Adrian, R., Friedrich, R., Nieuwstadt, F., 1994. Fully developed turbulent pipe flow: a comparison between direct numerical simulation and experiment. J. Fluid Mech. 268, 175–210.

El Khoury, G., Schlatter, P., Noorani, A., Fischer, P., Brethouwer, G., Johansson, A., 2013. Direct numerical simulation of turbulent pipe flow at moderately high Reynolds numbers. Flow Turbul. Combust. 91, 475–495.

Fischer, P.F., Lottes, J.W., Kerkemeier, S.G., 2008. nek5000 web page. http://nek5000.mcs.anl.gov.

Gärtner, D., Johannsen, K., Ramm, H., 1974. Turbulent heat transfer in a circular tube with circumferentially varying thermal boundary conditions. Int. J. Heat Mass Transfer 17, 1003–1018.

Irrenfried, C., Steiner, H., 2024. Modulation of turbulence flux budgets by varying fluid properties in heated high Prandtl number flow. Flow Turbul. Combust. 112 (1), 147–164.

Lee, J., Jung, S.Y., Sung, H.J., Zaki, T.A., 2013. Effect of wall heating on turbulent boundary layers with temperature-dependent viscosity. J. Fluid Mech. 726, 196–225.

Merchán, R.P., Santos, M.J., Medina, A., Calvo Hernández, A., 2022. High temperature central tower plants for concentrated solar power: 2021 overview. Renew. Sustain. Energy Rev. 155, 111828.

Piller, M., 2005. Direct numerical simulation of turbulent forced convection in a pipe. Internat. J. Numer. Methods Fluids 49, 583–602.

Pinelli, A., Uhlmann, M., Sekimoto, A., Kawahara, G., 2010. Reynolds number dependence of mean flow structure in square duct turbulence. J. Fluid Mech. 644, 107–122.

Pirozzoli, S., Modesti, D., Orlandi, P., Grasso, F., 2018. Turbulence and secondary motions in square duct flow. J. Fluid Mech. 840, 631–655.

Pirozzoli, S., Romero, J., Fatica, M., Verzicco, R., Orlandi, P., 2021. One-point statistics for turbulent pipe flow up to $Re_\tau \approx 6000$. J. Fluid Mech. 926, A28.

Prandtl, L., 1926. Über die ausgebildete turbulenz. In: NACA Tech. Memo.

Quarmby, A., Quirk, R., 1972. Measurements of the radial and tangential eddy diffusivities of heat and mass in turbulent flow in a plain tube. Int. J. Heat Mass Transfer 15, 2309–2327.

Redjem-Saad, L., Ould-Rouiss, M., Lauriat, D., 2007. Direct numerical simulation of turbulent heat transfer in pipe flows: effect of Prandtl number. Int. J. Heat Fluid Flow 28 (5), 847–861.

Reynolds, W.C., 1963. Turbulent heat transfer in a circular tube with variable circumferential heat flux. Int. J. Heat Mass Transfer 6, 445–454.

Rodríguez-Sánchez, M.R., Soria-Verdugo, A., Almendros-Ibáñez, J.A., Acosta-Iborra, A., Santana, D., 2014. Thermal design guidelines of solar power towers. Appl. Therm. Eng. 63 (1), 428–438.

Straub, S., Forooghi, P., Marocco, L., Wetzel, T., Frohnapfel, B., 2019. Azimuthally inhomogeneous thermal boundary conditions in turbulent forced convection pipe flow for low to medium Prandtl numbers. Int. J. Heat Fluid Flow 77, 352–358.

Sufrà, L., Steiner, H., 2022. Forced turbulent convection along heated and cooled walls with variable fluid properties. J. Fluids Eng. 144 (1), 011401.

Wu, X., Moin, P., 2008. A direct numerical simulation study on the mean velocity characteristics in turbulent pipe flow. J. Fluid Mech. 608, 81–112.

Zonta, F., Marchioli, C., Soldati, A., 2012. Modulation of turbulence in forced convection by temperature-dependent viscosity. J. Fluid Mech. 697, 150–174.